



Mg and K dual-decorated Fe-on-reduced graphene oxide for selective catalyzing CO hydrogenation to light olefins with mitigated CO₂ emission and enhanced activity



Yi Cheng^a, Jun Lin^b, Tijun Wu^a, Hao Wang^a, Songhai Xie^a, Yan Pei^a, Shirun Yan^a, Minghua Qiao^{a,*}, Baoning Zong^{c,*}

^a Collaborative Innovation Center of Chemistry for Energy Materials, Department of Chemistry and Shanghai Key Laboratory of Molecular Catalysis and Innovative Materials, Fudan University, Shanghai 200433, PR China

^b Key Laboratory of Nuclear Analysis Techniques, Shanghai Institute of Applied Physics, Chinese Academy of Sciences, Shanghai 201800, PR China

^c State Key Laboratory of Catalytic Materials and Chemical Engineering, Research Institute of Petroleum Processing, SINOPEC, Beijing 100083, PR China

ARTICLE INFO

Article history:

Received 6 September 2016

Received in revised form 9 November 2016

Accepted 26 November 2016

Available online 27 November 2016

Keywords:

Magnesium

Potassium

Iron/reduced graphene oxide

Fischer–Tropsch synthesis

Light olefins

ABSTRACT

One-step conversion of syngas (a mixture of CO and H₂) to C₂–C₄ light olefins (FTO) has attracted enormous attention in recent years because of the great improvement in process simplicity. However, on the documented FTO catalysts, the carbon efficiency is quite low (CO₂ selectivity as high as ~50%) and hence the green-house gas emission is high. Herein, we report about the design of novel Mg and K dual-decorated iron catalysts supported on reduced graphene oxide (rGO) to address this issue. We identified that on a dual-decorated FeMgK₂/rGO catalyst with the optimized amounts of Mg and K, not only the selectivity to light olefins amounted to 65.0%, but also the selectivity to CO₂ was appreciably cut down to 40.8%. On the basis of systematic characterizations, we propose that the suppression of the formation of magnetite during FTO because of Mg decoration effectively inhibited the water–gas shift (WGS) reaction, one of the main reaction pathways for CO₂ generation. Furthermore, successive decoration with only 0.50–2.0 wt% of K drastically boosted the iron time yield to hydrocarbons (FTY) to 1060–1706 μmol g_{Fe}⁻¹ s⁻¹ and the iron time yield to light olefins (FTY_{ole}) to 521–1003 μmol g_{Fe}⁻¹ s⁻¹. The new strategy of alkaline-earth metal-alkali metal dual decoration for the design of the iron-based catalysts may propel the development of a practical FTO process featuring high productivity and low CO₂ emission.

© 2016 Elsevier B.V. All rights reserved.

1. Introduction

Light olefins are key feedstocks in chemical industries for the manufacture of a wide range of products [1–5]. Currently, light olefins are mainly produced from steam cracking and fluid catalytic cracking of naphtha [6,7]. Regarding the sustainability of the carbon resource and our environment, strategies that start with syngas derived from non-petroleum carbon resources, such as natural gas, coal, and renewable biomass, for the production of light olefins are more appealing [2,7]. The syngas-based strategies for the production of light olefins are generally classified into (1) the indirect routes via methanol-to-olefins (MTO), dimethyl ether-to-

olefins (DMTO), and dehydration of lower alcohols, which require the synthesis of alcohols or dimethyl ether as intermediates, and (2) the direct route via FTO, which is economically more competitive by substituting the one-step route for the more complicated two-step routes [7].

FTO demands reaction temperatures (>573 K) higher than Fischer–Tropsch synthesis (FTS) to shift the products to low molecular-weight hydrocarbons, thereby affording the possibility to maximize the selectivity to light olefins [1,7]. However, the side effect of high temperature is that the WGS reaction, one of the main pathways for CO₂ generation [8,9], is kinetically accelerated simultaneously [10]. As a result, the CO₂ selectivities on the FTO catalysts are quite high. For instance, up to 50% of CO was converted to CO₂ on the Na and S decorated iron catalysts [6]. The CO₂ selectivity was 50.4% on the carbon nanotubes (CNTs) encapsulated iron catalyst at 573 K [11], and amounted to 56.0% on the pod-like CNT encapsulated iron catalyst [12]. On our K-decorated Fe/rGO cata-

* Corresponding authors.

E-mail addresses: mhqiao@fudan.edu.cn (M. Qiao), zongbn.ripp@sinopec.com (B. Zong).

lysts, the CO₂ selectivity was also about 50% [13]. The low carbon efficiency necessitates the development of a novel FTO catalyst that can effectively suppress the selectivity to CO₂, which will endow the FTO process with improved carbon atom economy and sustainability. Moreover, the removal of the O atom in CO in the form of H₂O instead of CO₂ is of significance for the commercialization of the FTO process in areas of water scarcity such as the Middle East and China.

In FTS for liquid fuel production, it was found that Mg could decrease the CO₂ selectivities on the cobalt- and iron-based catalysts. Niemelä and Krause reported that the Co/SiO₂ catalyst decorated with Mg reduced the generation of CO₂, which was tentatively attributed to the chemical modification of the active sites [14]. Luo and Davis studied the effects of the alkaline-earth metal promoters on the catalytic performances of the precipitated iron catalysts, and found that Mg suppressed the WGS reaction and consequently the formation rate of CO₂ [15]. A similar effect of Mg on the precipitated Fe/Cu/K/SiO₂ catalyst was reported by Li and co-workers [16]. However, the origin underlying the inhibitive effect of Mg on the WGS reaction is not clear.

In view of the function of Mg in FTS, it is a logical extension to use Mg in FTO to suppress CO₂ generation. In an earlier work, we demonstrated that the K-decorated Fe/rGO catalyst is highly active and selective to light olefins in FTO, which is largely due to the merits of the rGO support, such as large surface area, abundant defects, unique 2-dimensional structure, and excellent thermal conductivity [13]. Herein, we explored first the promotion effect of Mg on the Fe/rGO catalyst paying particular attention to CO₂ generation. Second, the FeMg/rGO catalyst with the optimal amount of Mg was decorated by K with the aim to develop an FTO catalyst bearing low CO₂ selectivity, high activity, and high selectivity to light olefins. The Mg and K dual-decorated Fe/rGO catalysts before and after FTO were comprehensively characterized, with which the specific effects of Mg and K on the catalytic performance in FTO were discussed.

2. Experimental

2.1. Catalyst preparation

GO was purchased from XF Nano Materials Technol. and used as received, which contained 1.8 wt% of S, 4.6 wt% of Cl, and 0.16 wt% of K determined on a Bruker AXS S4 Explorer X-ray fluorescence (XRF) scattering spectrometer. Other chemicals were of analytical grade and purchased from Sinopharm Chemical Reagent.

The Mg-decorated Fe/rGO catalysts were prepared by the coprecipitation method. Typically, 0.50 g GO was dispersed in 100 ml deionized water under ultrasonication for 2.5 h to yield a yellowish-brown suspension. Exactly 0.38 g FeCl₃·6H₂O and a desired amount of MgCl₂·6H₂O were dissolved in 10 ml deionized water, which was added dropwise to the suspension under vigorous stirring. The sticky suspension was stirred for 8 h and then heated to 353 K, to which 10 ml 85% hydrazine hydrate aqueous solution, acting as the reducing agent for GO and the precipitant for Fe³⁺ and Mg²⁺, was added dropwise. During the addition of hydrazine hydrate, the pH increased from 1.5 to 8.2. Then, about 6.0 ml 25% ammonia solution was added dropwise to adjust the pH to 9.0. The mixture was further refluxed at 353 K for 12 h. The resulting black solid was collected by filtration, washed repeatedly with deionized water, and dried at 333 K for 8 h. The Mg-decorated catalysts were denoted as FeMgx/rGO, in which x is the nominal molar percentage of Mg with respect to Fe. Specifically, FeMg28/rGO was also denoted as FeMg/rGO for brevity when subjected to K decoration. The Fe/rGO catalyst was prepared in the same way but in the absence of MgCl₂. Originated from hydrazine hydrate, the resulting catalysts con-

tained a small amount of N (1.8 wt%) as determined on a VARIO EL3 instrument (ELEMEN TAR), which is consistent with previous reports [13,17]. No impurities originally in GO were detected by XRF in the as-prepared catalysts after being subjected to the preparation procedures.

The Mg and K dual-decorated catalysts (FeMgK/rGO) were prepared by impregnating FeMg/rGO with K₂CO₃. After the washing step during the preparation of FeMg/rGO, the black cake (dry weight 0.41 g) was reslurried in 200 ml deionized water and ultrasonicated for 0.5 h. Then, a calculated volume of 5 mM K₂CO₃ aqueous solution was added to give the prescribed amount of K. The mixture was ultrasonicated for another 0.5 h and stirred for 12 h. After evaporation of excessive water at 333 K, the solid was further dried at 333 K for 8 h. The resulting catalysts were denoted as FeMgKy/rGO, in which y stands for the nominal weight percentage of K with respect to Fe.

2.2. Catalyst evaluation and product analysis

The as-prepared catalysts were pelletized, crushed, and sieved to 60–80 meshes. Exactly 0.10 g catalyst was diluted with 0.80 g quartz powders (60–80 meshes) and loaded in a tubular fixed-bed reactor with an inner diameter of 10 mm. Prior to FTO, the catalyst was reduced in flowing H₂/Ar (5 vol.%, 50 ml min⁻¹) at 723 K for 16 h with a heating rate of 2 K min⁻¹. Catalytic evaluation was performed under the reaction conditions of 613 K, 20 bar, and a H₂/CO/N₂ volume ratio of 48/48/4, with N₂ as the internal standard.

Analysis of the FTO products was conducted online using two gas chromatographs fitted with two high-temperature high-pressure Valco six-port valves. H₂, N₂, CO, CH₄, and CO₂ in the gas phase were analyzed on a GC122 gas chromatograph equipped with a 2 m-long TDX-01 packed stainless steel column connected to a thermal conductivity detector (TCD). The hydrocarbons were analyzed on a GC9560 gas chromatograph equipped with a PONA capillary column (50 m × 0.25 mm × 0.50 μm) connected to a flame ionization detector (FID). Since the C₂H₄/C₂H₆ and C₃H₆/C₃H₈ pairs cannot be neatly separated by the PONA capillary column, their relative ratios were determined on the GC122 gas chromatograph equipped with a PoraPlot Q capillary column (12.5 m × 0.53 mm × 20 μm) connected to a FID. The catalytic activity (FTY) was expressed as the moles of CO converted to hydrocarbons per gram Fe per second. The productivity of light olefins (FTY_{ole}) was expressed as the moles of CO converted to light olefins per gram Fe per second. The hydrocarbon selectivities were calculated on carbon basis with the exception of CO₂. The carbon balances of the FTO products in all catalytic runs were within 92–105%.

2.3. Characterization

The loadings of Fe, Mg, and K were determined by the inductively coupled plasma-atomic emission spectroscopy (ICP-AES; Thermo Elemental IRIS Intrepid). The multipoint Brunauer–Emmett–Teller surface area (S_{BET}), pore volume (V_{pore}), and average pore diameter (d_{pore}) were measured by N₂ physisorption on a Micromeritics TriStar3000 apparatus at 77 K. The catalyst was pretreated at 473 K under flowing N₂ for 8 h.

The conventional powder X-ray diffraction (XRD) pattern was acquired on a Bruker AXS D8 Advance X-ray diffractometer using Ni-filtered Cu K α radiation ($\lambda = 0.15418$ nm). The tube voltage was 40 kV, and the current was 40 mA. The 2θ angles were scanned from 20 to 80° at 1° min⁻¹ with the step size of 0.01°. The catalyst was protected by PEG200 during data acquisition to avoid oxidation. The synchrotron-radiation powder XRD pattern was collected on a Huber5021 six-circle diffractometer at BL14B1 beamline at the Shanghai Synchrotron Radiation Facility (SSRF). The X-ray beam wavelength (λ) was set to 0.12398 nm by a Si(111) channel-

cut monochromator. The synchrotron-radiation XRD pattern was converted to 2θ values corresponding to the Cu K α radiation to facilitate phase identification.

The Fe K-edge X-ray absorption near-edge structure (XANES) was recorded in the transmission mode on the 1W1B beamline at the Beijing Synchrotron Radiation Facility (BSRF). The typical electron beam energy was 2.5 GeV, and the current was 200 mA. The beamline was equipped with a Si(111) double crystal monochromator. Ionization chambers were used to detect the incident and transmitted beams.

The surface morphology and particle size distribution (PSD) were observed by transmission electron microscopy (TEM) on a JEOL JEM2011 microscope operated at 200 kV. The catalyst was ground in an agate mortar with anhydrous ethanol, ultrasonicated, and dripped onto a carbon film-coated copper grid. The PSD histogram was constructed by randomly measuring at least 300 particles. The as-prepared FeMgK2/rGO was additionally characterized by scanning transmission electron microscopy-energy dispersive spectroscopy (STEM-EDS) to locate the distributions of C, O, Fe, Mg, and K under the STEM mode. The microstructure of FeMgK2/rGO after 24 h on stream in FTO was observed by high-resolution TEM (HRTEM). Both STEM-EDS and HRTEM characterizations were conducted on a FEI Tecnai G2 S-Twin F20 field-emission transmission electron microscope operated at 200 kV with an Oxford Instrument X-Max 80T EDS detector.

X-ray photoelectron spectroscopy (XPS) was conducted on a Kratos Axis Ultra Dld XPS spectrometer using Al K α radiation ($h\nu = 1486.6$ eV) as the excitation source. The pass energy was 160 eV for survey scans and 40 eV for selected regions. The Raman spectrum was recorded on a Horiba Jobin Yvon XploRA Raman spectrometer using a 12.5 mW laser source at an excitation wavelength of 532 nm. The spectral resolution was 1.8 cm^{-1} .

Temperature-programmed desorption (TPD) of CO, H₂, and CO₂ was performed on a Micromeritics 2750 chemisorption system. The carrier gas was He in CO- and CO₂-TPD and Ar in H₂-TPD. The weighed catalyst (~0.10 g) loaded in a U-shaped quartz tube was reduced on site at 723 K for 16 h under flowing H₂/Ar (5 vol.%, 50 ml min⁻¹). After being cooled down to 298 K, pure CO, H₂, or CO₂ pulses were injected until the eluted peak did not change in intensity as monitored by TCD. The catalyst was then purged with the carrier gas (25 ml min⁻¹) for at least 40 min to remove the gaseous and physisorbed adsorbate until the signal returned to the baseline. The TPD curve was acquired by heating the catalyst from 300 to 723 K at a heating rate of 10 K min⁻¹. The amount of the desorbed adsorbate was monitored by TCD. Comparison of the area of the desorption peak with that calibrated by a 100 μl -capacity loop using the corresponding adsorbate allowed for the purpose of quantification.

⁵⁷Fe Mössbauer absorption spectra were recorded in the constant acceleration transmission mode at room temperature on a Wissel 1550 electromechanical spectrometer (Wissenschaftliche Elektronik GmbH) using a ⁵⁷Co/Pd irradiation source. The velocity was calibrated by a 25 μm -thick α -Fe foil, and the isomer shift (IS) was referenced to α -Fe at room temperature. The spectrum was fitted using the least-squares fitting routine that modeled the spectrum as appropriate superpositions of quadrupole doublets and magnetic sextets with Lorentzian line shape and constrains in peak width and relative intensity using the MossWinn 3.0i program. The derived hyperfine parameters, including IS, QS (quadrupole shift for sextet or quadrupole splitting for doublet), and magnetic hyperfine field (H), were used for spectral component qualification. The phase compositions were calculated from the areas of the absorption peaks with the assumption of the same recoil-free factor (the probability of absorption of γ -ray) for all kinds of iron nuclei [18].

3. Results

3.1. Effect of Mg decoration on FTO

Table 1 summarizes the FTO results over the Fe/rGO catalysts decorated with different amounts of Mg under the industrially relevant conditions of 613 K, 20 bar, and a H₂/CO ratio of 1. On Mg-free Fe/rGO, the FTY was $342 \mu\text{mol}_{\text{CO}} \text{ g}_{\text{Fe}}^{-1} \text{ s}^{-1}$, and the CO₂ selectivity was 49.7%. The FTY increased initially on FeMg7/rGO, and then decreased steadily with the increase in the amount of Mg. The CO₂ selectivity declined throughout the amount of Mg investigated to 38.7% on FeMg42/rGO, validating the idea that similar to the effect of Mg on iron-based catalysts [15,16] and cobalt-based catalysts in FTS [14,19], Mg is also an effective promoter in suppressing CO₂ generation in FTO.

To investigate the effect of the way of Mg decoration, two additional catalysts with the same amount of Mg as FeMg28/rGO were prepared, as FeMg28/rGO displayed much higher FTY than FeMg42/rGO and the second-lowest CO₂ selectivity of 40.7% (**Table 1**). One is FeMg28/rGO-IM that was prepared by impregnating Mg(NO₃)₂ on Fe/rGO followed by calcination at 623 K for 4 h under flowing N₂, and the other is FeMg28/rGO-C that was prepared by using Na₂CO₃ as the precipitant for FeCl₃ and MgCl₂ and hydrazine hydrate as the reductant for GO. **Table 1** shows that on FeMg28/rGO-IM, the CO₂ selectivity declined to 42.3%, but the FTY, O/P ratio, and FTY_{ole} were far inferior to those on FeMg28/rGO. On FeMg28/rGO-C, the CO₂ selectivity declined to 41.1%, and the FTY, O/P ratio, and FTY_{ole} were higher than those on FeMg28/rGO-IM, but still lower than those on FeMg28/rGO.

We also prepared FeCa28/rGO-C, FeSr28/rGO-C, and FeBa28/rGO-C in the way identical to that of FeMg28/rGO-C using corresponding metal chlorides to explore the promotion effects of other alkaline-earth metals. As compiled in **Table 1**, analogous to Mg, these alkaline-earth metals are capable of suppressing the generation of CO₂, but the effectiveness descended in the order of Mg > Ca > Sr > Ba. The FTY and FTY_{ole} also followed this order, manifesting that Mg is the most suitable promoter among the alkaline-earth metals as far as the CO₂ selectivity and the FTO activities are concerned.

3.2. Effect of Mg and K dual decoration on FTO

Although the CO₂ selectivity was effectively suppressed on FeMg28/rGO, its moderate FTY, high CH₄ selectivity, and low selectivity to light olefins (**Table 1**) necessitate further catalyst modification. Since K has been proven as a promising promoter to eliminate these shortcomings [13,20,21], FeMg28/rGO was further decorated with K. The catalytic results over the Mg and K dual-decorated Fe/rGO catalysts with various amounts of K under the industrially relevant conditions of 613 K, 20 bar, and a H₂/CO ratio of 1 are summarized in **Table 2**. It is fortunate that the beneficial effect of Mg in suppressing the generation of CO₂ was not affected by K and irrespective of the amount of K, suggesting that only Mg modified the pathway for CO₂ generation on the FeMgK/rGO catalysts. It should be reminded that the CO₂ selectivities on the FeMgK/rGO catalysts at the CO conversion levels of 59–62% are comparable to that of 40–45% on the novel ZnCrO_x–MSAPO bifunctional catalyst for FTO at CO conversion of ~17% [2], and are lowered by ~20% relative to those reported on iron-based FTO catalysts [6,11–13,22].

It is surprising but unambiguous that with the decoration of only 0.50 wt% of K, the FTY was boosted to 4.3 folds of that on FeMg/rGO. On FeMgK1/rGO, the FTY further increased to $1706 \mu\text{mol}_{\text{CO}} \text{ g}_{\text{Fe}}^{-1} \text{ s}^{-1}$, which is the highest value ever reported on the iron-based FTO catalysts [1,6,11–13,20,22–31]. It is worth noting that the amount of 1.0 wt% K leading to the highest FTO activity is in-between the optimal K loading of 0.7 wt% on precipitated FeMn

Table 1The FTO results over the alkaline-earth metal-decorated Fe/rGO catalysts.^a

Catalyst	FTY ($\mu\text{mol g}_{\text{Fe}}^{-1} \text{s}^{-1}$)	Space velocity ($\text{lg}^{-1} \text{h}^{-1}$)	S_{CO_2} (%)	Hydrocarbon selectivity ^b (wt%)				O/P	FTY _{ole} ($\mu\text{mol g}_{\text{Fe}}^{-1} \text{s}^{-1}$)
				CH ₄	C ₂ –C ₄ olefins	C ₂ –C ₄ paraffins	C ₅₊		
Fe/rGO	342	42	49.7	42.3	33.2	23.4	1.1	1.4	114
FeMg7/rGO	535	60	45.2	39.2	34.2	22.9	3.7	1.5	182
FeMg14/rGO	462	48	43.8	37.7	34.1	24.5	3.7	1.4	161
FeMg28/rGO	247	24	40.7	35.6	33.0	26.9	4.5	1.2	86
FeMg42/rGO	63	6	38.7	34.6	22.7	37.9	4.8	0.6	14
FeMg28/rGO-IM	31	3	42.3	32.1	24.8	41.5	1.6	0.6	42
FeMg28/rGO-C	202	18	41.1	36.6	27.7	34.6	1.1	0.8	56
FeCa28/rGO-C	182	18	43.0	37.0	23.0	38.2	1.8	0.6	42
FeSr28/rGO-C	127	12	44.7	38.7	27.7	30.8	2.8	0.9	35
FeBa28/rGO-C	116	12	46.0	38.3	17.3	43.2	1.2	0.4	20

^a Reaction conditions: 0.10 g catalyst, 613 K, 20 bar, H₂/CO = 1, and TOS = 24 h; data reported at CO conversion levels between 58 and 64%.^b Hydrocarbon selectivities are normalized with the exception of CO₂.**Table 2**The FTO results over the FeMg/rGO, FeMgK/rGO, and FeK/rGO catalysts.^a

Catalyst	FTY ($\mu\text{mol g}_{\text{Fe}}^{-1} \text{s}^{-1}$)	Space velocity ($\text{lg}^{-1} \text{h}^{-1}$)	S_{CO_2} (%)	Hydrocarbon selectivity ^b (wt%)				O/P	FTY _{ole} ($\mu\text{mol g}_{\text{Fe}}^{-1} \text{s}^{-1}$)
				CH ₄	C ₂ –C ₄ olefins	C ₂ –C ₄ paraffins	C ₅₊		
FeMg/rGO	247	24	40.7	35.6	33.0	26.9	4.5	1.2	86
FeMgK0.5/rGO	1060	102	40.5	31.4	49.2	13.5	5.9	3.6	521
FeMgK1/rGO	1706	168	41.1	27.1	58.8	7.7	6.4	7.6	1003
FeMgK2/rGO	1338	132	40.8	20.3	65.0	6.2	8.5	10.5	869
FeMgK5/rGO	617	54	40.5	19.6	64.2	5.9	10.3	10.9	396
FeK2/rGO	545	60	49.0	22.0	63.7	6.4	7.9	10.0	346

^a Reaction conditions: 0.10 g catalyst, 613 K, 20 bar, H₂/CO = 1, and TOS = 24 h; data reported at CO conversion levels between 59 and 62%.^b Hydrocarbon selectivities are normalized with the exception of CO₂.

[32] and 1.5 wt% on FeMnCuSi in FTS [33]. Further improving the amount of K decreased the FTY. The volcanic evolution of the activity with the amount of K has been observed on the K-decorated Mn/FeN/CNT [25] and Fe/rGO in FTO [13], but the extents of the activity enhancement were much less drastic, which strongly evidence that Mg can enhance the promotion effect of K on activity when they coexist, though Mg alone is adverse to the activity.

To further discriminate the roles of Mg and K in FTO, we prepared FeK2/rGO by decorating Fe/rGO with 2.0 wt% K as a control catalyst. Table 2 shows that the CO₂ selectivity on FeK2/rGO was similar to that on Fe/rGO, proving again that K did not affect the generation of CO₂. The FTY on FeK2/rGO was higher than that of Fe/rGO, but far inferior to that of FeMgK2/rGO, substantiating that the excellent activity of the dual-decorated FeMgK/rGO catalysts is a result of the synergistic effect between Mg and K.

K decoration not only enhanced the activity, but also improved the selectivity to light olefins. The selectivity to light olefins increased with the amount of K at first, passed through a maximum of 65.0% on FeMgK2/rGO, and then decreased marginally to 64.2% on FeMgK5/rGO. Similarly, the O/P ratio increased from 1.2 on FeMg/rGO to 10.5 on FeMgK2/rGO, and then increased minimally on FeMgK5/rGO. Although the selectivity to light olefins on FeMgK2/rGO is lower than the value of 80% on the ZnCrO_x–MSAPO bifunctional catalyst [2], it is substantially higher than those on K/Mn/FeN/CNT (43.6%) [25], Fe/NCNT (46.7%) [20], Fe/NG (49.6%) [23], Na and S decorated Fe/α-Al₂O₃ (53%) [1], and Mn/Fe₃O₄ microsphere (60.1%) [34]. Despite a higher selectivity to light olefins of 68% was reported on a hierarchically structured Fe/α-Al₂O₃ catalyst decorated with S, that value was acquired at the CO conversion of only 0.9% [27]. The present work successfully demonstrates that reduced CO₂ emission, enhanced activity, and high selectivity to light olefins can be achieved simultaneously on a state-of-the-art FeMgK/rGO catalyst with suitable promoter combination. Table 2 also shows that the hydrocarbon distributions on FeK2/rGO and FeMgK2/rGO are similar, indicating that in FeMgK2/rGO only K tailored the selectivities to the hydrocarbons.

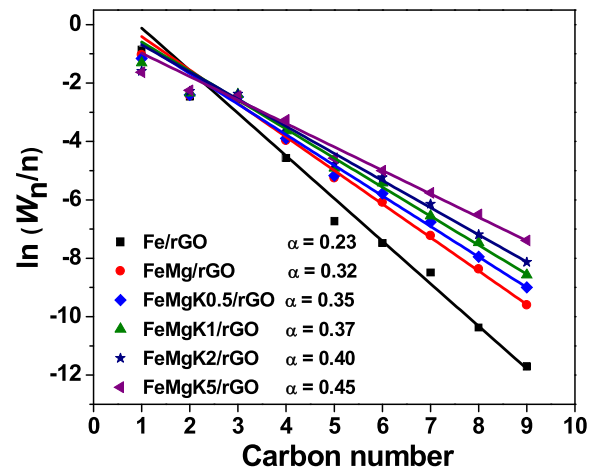


Fig. 1. ASF plots of the Fe/rGO, FeMg/rGO, and FeMgK/rGO catalysts.

Fig. 1 presents the Anderson–Schulz–Flory (ASF) plots of the FeMg/rGO and K-decorated FeMg/rGO catalysts. The chain-growth probability (α) increased from 0.23 to 0.45 with the amount of K from 0 to 5.0 wt%. The α value less than 0.3 favors the production of CH₄, while larger than 0.5 favors the production of C₅₊ hydrocarbons [35], which accounts for the decrease in the selectivity to CH₄ and the increase in the selectivity to the C₅₊ hydrocarbons with the increase in the amount of K (Table 2). On FeMgK2/rGO and FeMgK5/rGO, their α values fell in the optimal range of 0.4–0.5 for the production of C₂–C₄ hydrocarbons [7], thus affording the highest selectivities to light olefins.

3.3. Stability of FeMgK2/rGO in FTO

In view of the excellent catalytic performance of FeMgK2/rGO, it was subjected to a 120 h stability testing in FTO. The space velocity was adjusted to 721 g⁻¹ h⁻¹ to render an initial CO conversion of

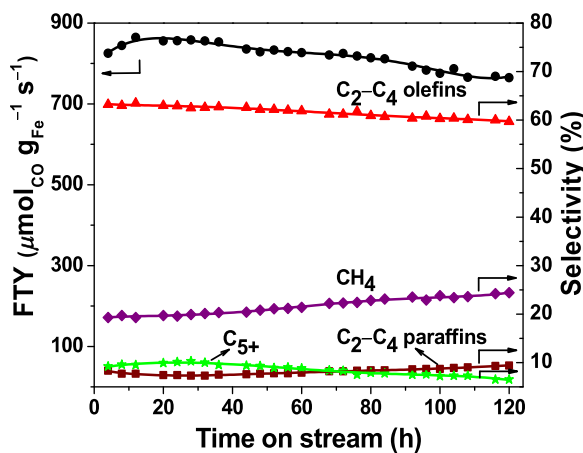


Fig. 2. The FTO results over the FeMgK2/rGO catalyst during 120 h on stream under the reaction conditions of 0.10 g catalyst, 613 K, 20 bar, a H_2/CO ratio of 1, and the space velocity of $721 \text{ g}^{-1} \text{ h}^{-1}$.

76.5% to facilitate a direct comparison with the stability of $\text{Fe}/\alpha\text{-Al}_2\text{O}_3$ decorated with Na and S [1] and FeK1/rGO [13] with the stability being tested at similar conversion level. Fig. 2 shows that the FTY increased slightly with time on stream (TOS) and reached the maximum of $865 \mu\text{mol}_{\text{CO}} \text{ g}_{\text{Fe}}^{-1} \text{ s}^{-1}$ within 12 h. Then, the FTY declined slowly and retained at $765 \mu\text{mol}_{\text{CO}} \text{ g}_{\text{Fe}}^{-1} \text{ s}^{-1}$ after 120 h on stream. As for the distribution of the hydrocarbons, the selectivity to light olefins decreased slightly from 63.2 to 59.7%, whereas

that to CH_4 increased slowly from 19.3 to 24.4% after 120 h on stream. At the first sight, FeMgK2/rGO is as stable as $\text{Fe}/\alpha\text{-Al}_2\text{O}_3$ decorated with Na and S [1] and FeK1/rGO [13]. However, it should be pointed out that the space velocity and FTY were much higher for FeMgK2/rGO during the stability testing.

3.4. Composition, texture, and microstructure

To understand the promotion effects of Mg and K, the as-prepared Fe/rGO , FeMg/rGO , and FeMgK/rGO catalysts were systematically characterized. Elemental analysis revealed that the practical Fe loading on Fe/rGO was 20.3 wt%. For the FeMg/rGO and FeMgK/rGO catalysts, the practical Mg/Fe molar ratios were around 0.31 (Table S1), which is slightly larger than the nominal ratio of 0.28. The practical K loadings on the FeMgK/rGO catalysts were in good agreement with the nominal loadings. On the other hand, Mg decoration improved the S_{BET} and V_{pore} , which complies with the effect of Mg on the fused iron catalyst [36]. For the Mg and K dual-decorated catalysts, the S_{BET} increased steadily up to 2.0 wt% of K. Then, the S_{BET} and V_{pore} decreased, while the d_{pore} increased for FeMgK5/rGO , signifying the blockage of some small pores by excessive K.

Fig. 3a presents the XRD patterns of the as-prepared catalysts. Similar to our previous work [13], the diffraction peaks are readily assigned to rGO and hematite ($\alpha\text{-Fe}_2\text{O}_3$, JCPDS 33-0664). The formation of hematite is further corroborated by XANES and HRTEM. Fig. 3b shows that the Fe K-edge photon energies (7124.0 eV) of the catalysts are identical to that of the hematite standard [37]. Fig. 3c reveals the lattice fringes with the spacing (d) of 2.52 \AA due to the

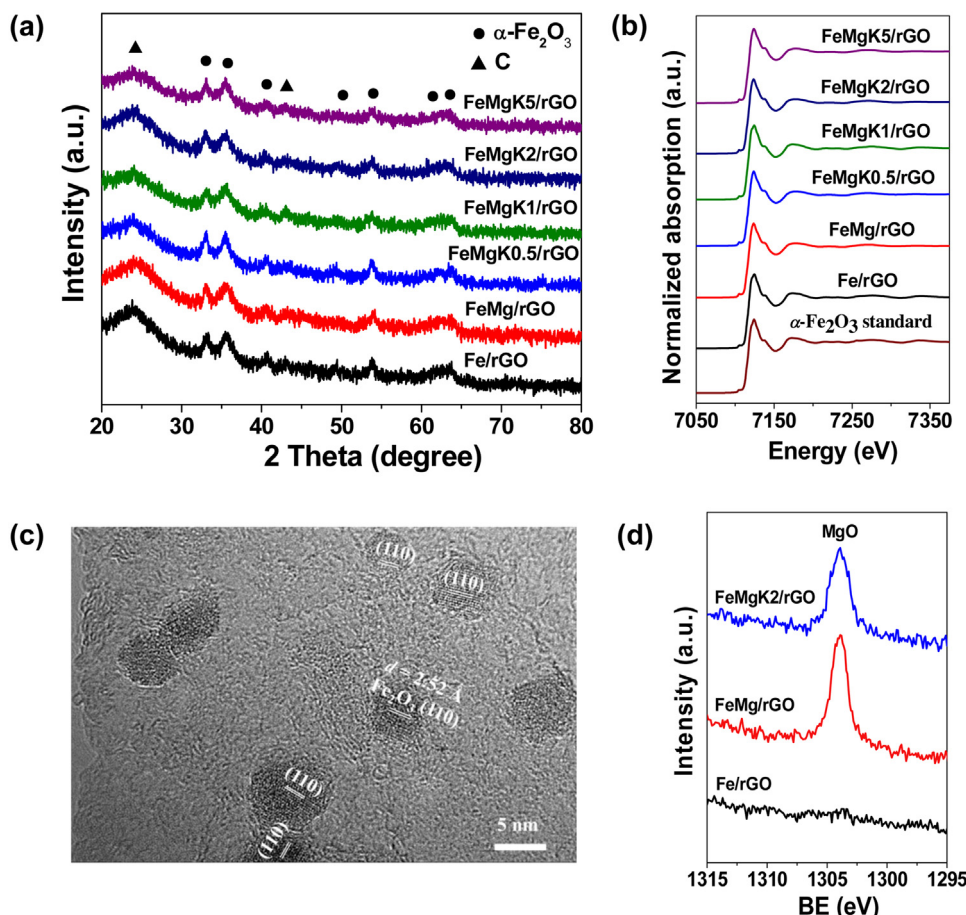


Fig. 3. (a) XRD patterns and (b) Fe K-edge XANES spectra of the Fe/rGO , FeMg/rGO , and FeMgK/rGO catalysts. The Fe K-edge XANES spectrum of the $\alpha\text{-Fe}_2\text{O}_3$ standard is included in (b) as a reference. (c) HRTEM image of the FeMgK2/rGO catalyst. (d) Mg 1s spectra of Fe/rGO , FeMg/rGO , and FeMgK2/rGO catalysts.

(110) planes of $\alpha\text{-Fe}_2\text{O}_3$ [38] taking FeMgK2/rGO as an example. No diffraction peaks from the Mg- and K-containing phases were visible in Fig. 3a, indicating their small sizes and high dispersion of Mg, and consistent with the small amounts of K. Although K was also not detected by XPS, the identity of Mg was successfully ascertained by XPS. As shown in Fig. 3d, FeMg/rGO and FeMgK2/rGO displayed a distinct Mg 1 s peak at the BE of 1303.8 eV ascribable to MgO [39].

The Raman spectra of the as-prepared catalysts (Fig. S1a) shows a D band at 1350 cm^{-1} and a G band at 1590 cm^{-1} characteristic of rGO [13]. On the basis of the wavenumber of the second-order Raman peak of around 2690 cm^{-1} (Fig. S1b), the thickness of rGO in these catalysts was estimated as <5 layers [40]. There are no discernable shifts in the Raman bands and no significant changes in the I_D/I_G ratios (Table S1), hence it is justified to exclude the possible impact of rGO on the differences in the FTO performances for these catalysts.

Fig. 4 shows the TEM images and PSD histograms of the as-prepared catalysts. The sheet-like morphology with typical wrinkle of graphene was clearly visualized, with the nanosheets being loaded with well-dispersed $\alpha\text{-Fe}_2\text{O}_3$ nanoparticles (NPs). The average size of the $\alpha\text{-Fe}_2\text{O}_3$ NPs on Fe/rGO was 8.0 nm, which was reduced to 7.4 nm on FeMg/rGO. Successive decoration with K did not induce significant change in the particle size. These size changes agree with previous observations that Mg decoration led to smaller iron particles [16], whereas K decoration did not affect the particle size of iron [41].

The STEM-EDS characterization was carried out using FeMgK2/rGO as a representative. Fig. 5a is the STEM image and Fig. 5b–f are the corresponding EDS mappings of C, O, Fe, Mg, and K. Comparison of Fig. 5a with Fig. 5c and d readily discloses that the bright particles are $\alpha\text{-Fe}_2\text{O}_3$ NPs. Furthermore, comparison of Fig. 5e and f with Fig. 5b or d reveals that Mg and K are located preferentially on or in vicinity to the $\alpha\text{-Fe}_2\text{O}_3$ NPs rather than distributed randomly on rGO, suggesting that Mg and K directly interact with Fe.

3.5. Adsorption behaviors of CO and H_2

The CO-TPD profiles of the Fe/rGO, FeMg/rGO, and FeMgK/rGO catalysts after reduction are presented in Fig. 6a. The CO desorption temperature was $\sim 377\text{ K}$ on Fe/rGO, which shifted down to 370 K on FeMg/rGO. The desorption temperature then increased from 379 to 386 K with the amount of K from 0.50 to 2.0 wt%. On FeMgK5/rGO, the main peak shifted back to 376 K , and a shoulder peak emerged at about 450 K . Accordingly, the CO adsorption capacity was $189\text{ }\mu\text{mol g}_{\text{cat}}^{-1}$ on Fe/rGO, and dropped to $115\text{ }\mu\text{mol g}_{\text{cat}}^{-1}$ on FeMg/rGO. The reduced CO adsorption capacity by Mg decoration may be attributed to the inhibition effect of MgO on the reduction of iron [16], which depleted the adsorption sites for CO. Besides, Lahtinen et al. reported that MgO directly covered the adsorption sites of CO on cobalt [42], an effect that is also expected to occur on FeMg/rGO, as MgO itself does not adsorb CO [36]. The CO adsorption capacity then recovered to $233\text{ }\mu\text{mol g}_{\text{cat}}^{-1}$ on FeMgK0.5/rGO, and kept on increasing with the amount of K (Fig. 6c). The promotion effect of K on CO adsorption is in line with the literature works [20,43,44], which was attributed to the role of K in facilitating electron donation from iron to CO [45].

The H_2 -TPD profiles are presented in Fig. 6b. All catalysts displayed a main desorption peak below 370 K from the weakly chemisorbed H_2 , along with a broad feature at about 600 K from the strongly chemisorbed H_2 [44]. The main peak shifted gradually to higher temperatures after Mg decoration and followed by K decoration. After decorating Fe/rGO with Mg, the H_2 adsorption capacity decreased slightly from 59.3 to $53.5\text{ }\mu\text{mol g}_{\text{cat}}^{-1}$, then increased steadily with the amount of K (Fig. 6c). Similar to its effect on the

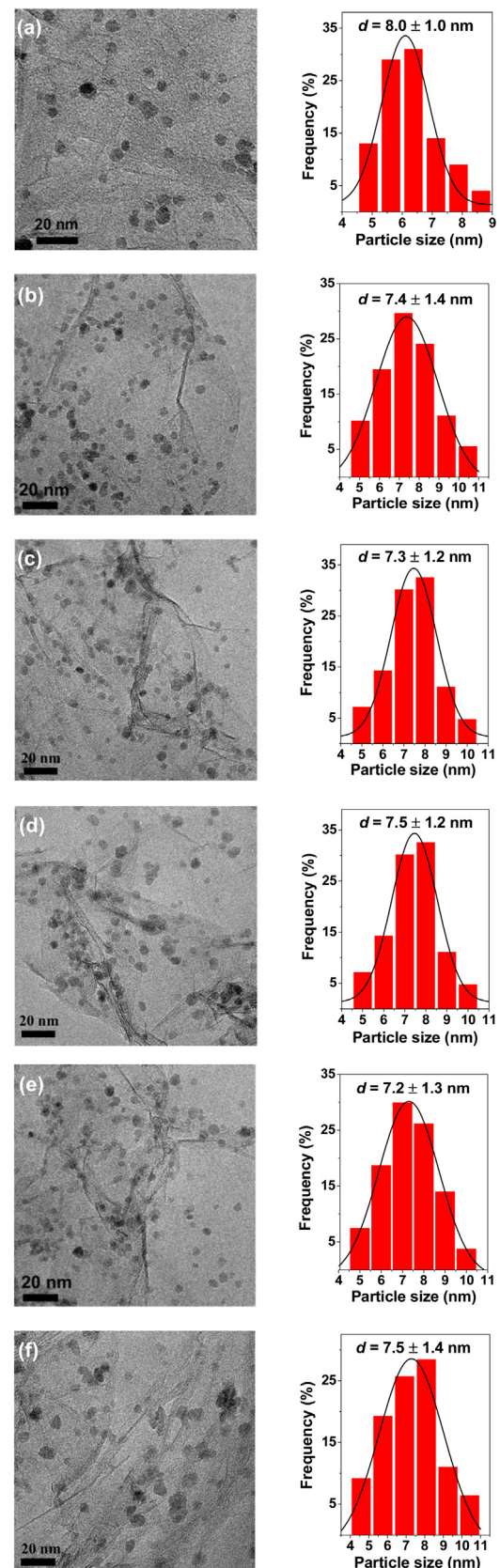


Fig. 4. TEM images and PSD histograms with Gaussian analysis fittings of the $\alpha\text{-Fe}_2\text{O}_3$ NPs of the (a) Fe/rGO, (b) FeMg/rGO, (c) FeMgK0.5/rGO, (d) FeMgK1/rGO, (e) FeMgK2/rGO, and (f) FeMgK5/rGO catalysts.

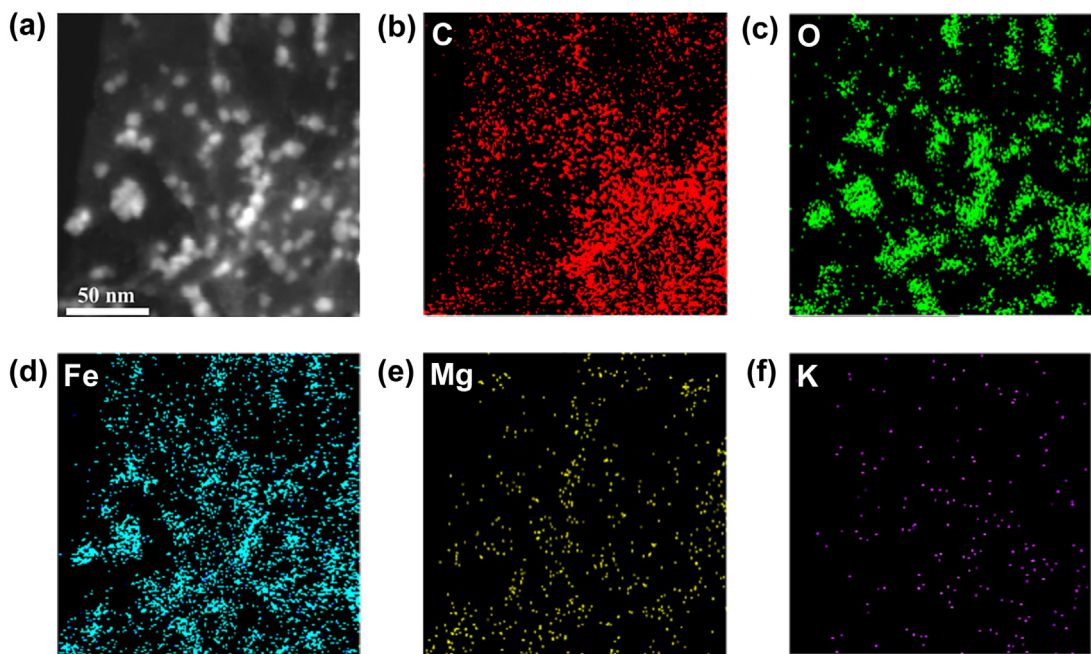


Fig. 5. (a) STEM image, and (b–f) EDS mappings of C, O, Fe, Mg, and K, respectively, of the as-prepared FeMgK₂/rGO catalyst.

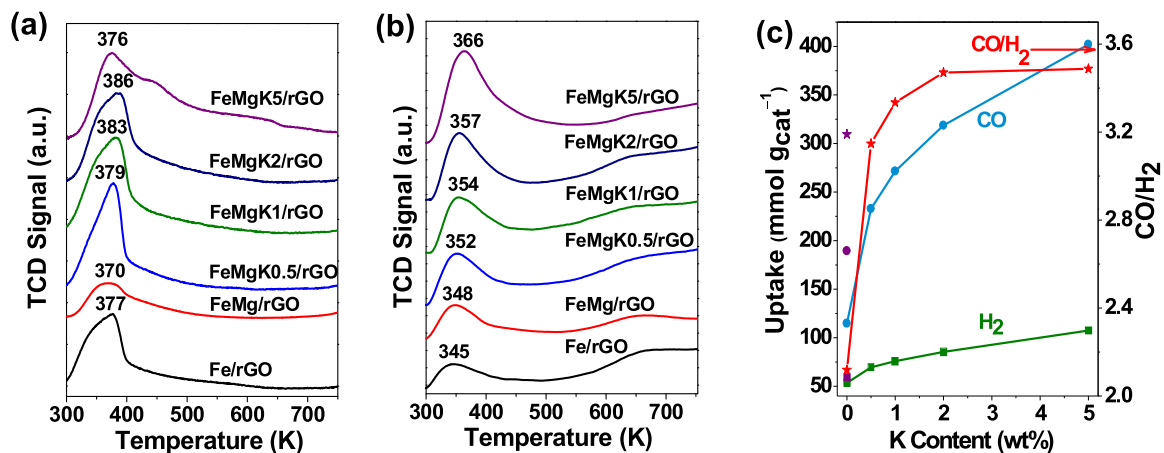


Fig. 6. (a) CO- and (b) H₂-TPD profiles of the Fe/rGO, FeMg/rGO, and FeMgK/rGO catalysts. (c) Adsorption capacities of CO and H₂ and the surface CO/H₂ ratios against the K content relative to FeMg/rGO; the purple symbols represent the adsorption capacities of the gases and the CO/H₂ ratio of Fe/rGO. (For interpretation of the references to color in this figure legend, the reader is referred to the web version of this article.)

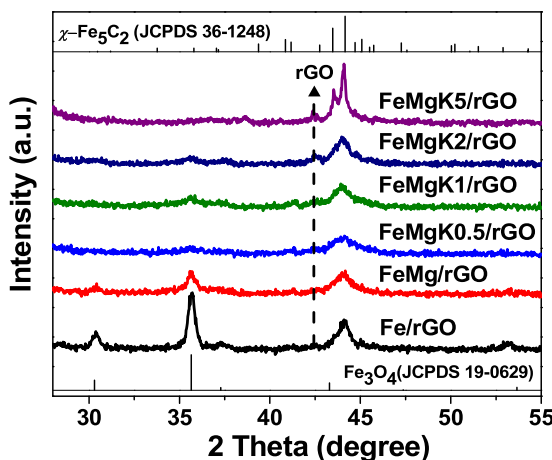


Fig. 7. Synchrotron-radiation XRD patterns of the Fe/rGO, FeMg/rGO, and FeMgK/rGO catalysts after 24 h on stream in FTO.

CO adsorption capacity, K also compensated for the loss of the H₂ adsorption capacity upon Mg decoration.

As illustrated in Fig. 6c, the surface CO/H₂ ratios derived from Fig. 6a and b follow the order of FeMg/rGO < Fe/rGO < FeMgK_{0.5}/rGO, which coincides with the orders of the selectivities to light olefins and the O/P ratios on these catalysts (Table 2). The improved surface CO/H₂ ratio is adverse to the secondary hydrogenation of light olefins, thus rendering high selectivity to light olefins at the expense of the C₂–C₄ paraffins [13,20,21]. When the amount of K increased from 2.0 to 5.0 wt%, there was only a minor increase in the surface CO/H₂ ratio, which is coherent with the small increments of the selectivity to light olefins and the O/P ratio (Table 2). Thus, it can be concluded that the selectivities to light olefins and the O/P ratios are closely related to the surface CO/H₂ ratios that are governed by K.

3.6. Phase composition and morphology after FTO

The Fe/rGO, FeMg/rGO, and FeMgK/rGO catalysts after 24 h on stream in FTO were examined by synchrotron-radiation XRD.

Fig. 7 shows that after reaction, Fe/rGO is constituted by magnetite (Fe_3O_4 , JCPDS 19-0629) and Hägg carbide ($\chi\text{-Fe}_5\text{C}_2$, JCPDS 36-1248). $\chi\text{-Fe}_5\text{C}_2$ has been proposed as the active phase in FTO [1,13,24,28]. Note that the features due to magnetite were attenuated on FeMg/rGO and almost diminished on the dual-decorated FeMgK/rGO catalysts. The broad feature at 2θ of $\sim 44^\circ$ from $\chi\text{-Fe}_5\text{C}_2$ declined in intensity for FeMg/rGO and FeMgK0.5/rGO, and then intensified at higher amounts of K. For FeMgK5/rGO, two sharp peaks at 2θ of 43.4 and 44.1° corresponding to the (021) and (510) reflections of $\chi\text{-Fe}_5\text{C}_2$, respectively, were resolved. On the basis of the broadening of the most intensive (510) peak and the Scher-

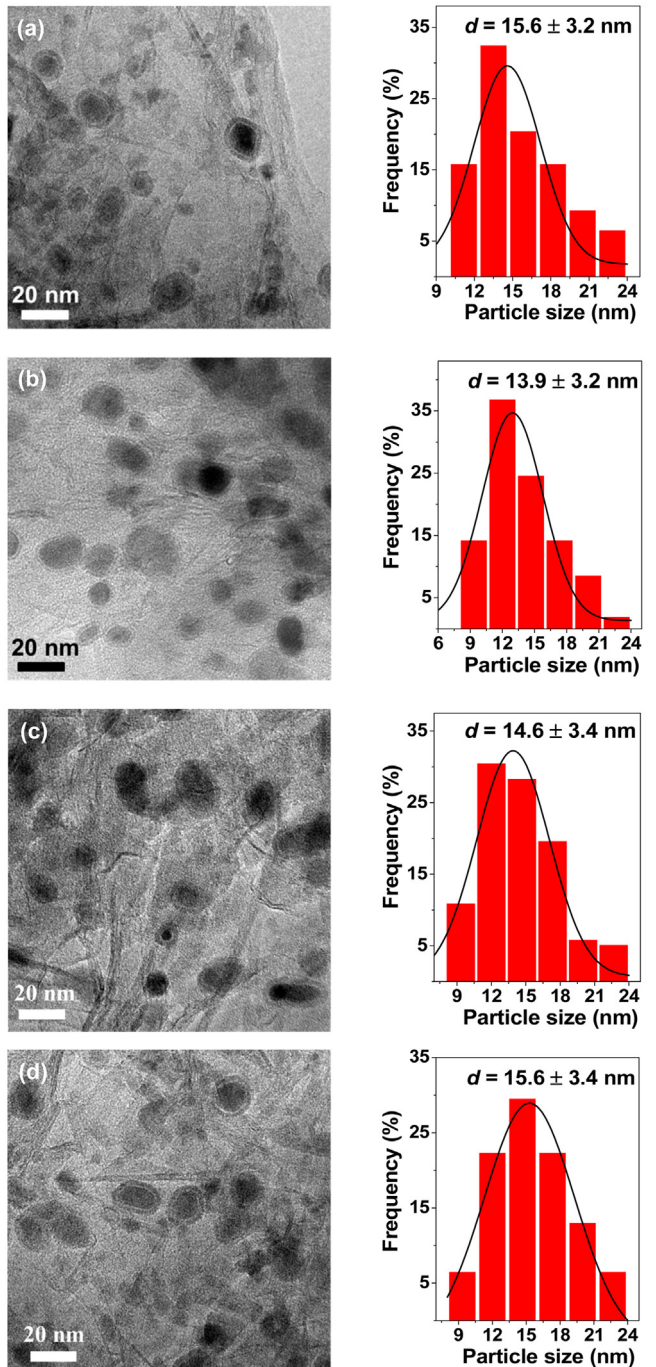


Fig. 8. TEM images and PSD histograms with Gaussian analysis fittings of the (a) Fe/rGO, (b) FeMg/rGO, (c) FeMgK0.5/rGO, (d) FeMgK1/rGO, (e) FeMgK2/rGO, and (f) FeMgK5/rGO catalysts after 24 h on stream in FTO. (g) HRTEM image of the FeMgK2/rGO catalyst after 24 h on stream in FTO.

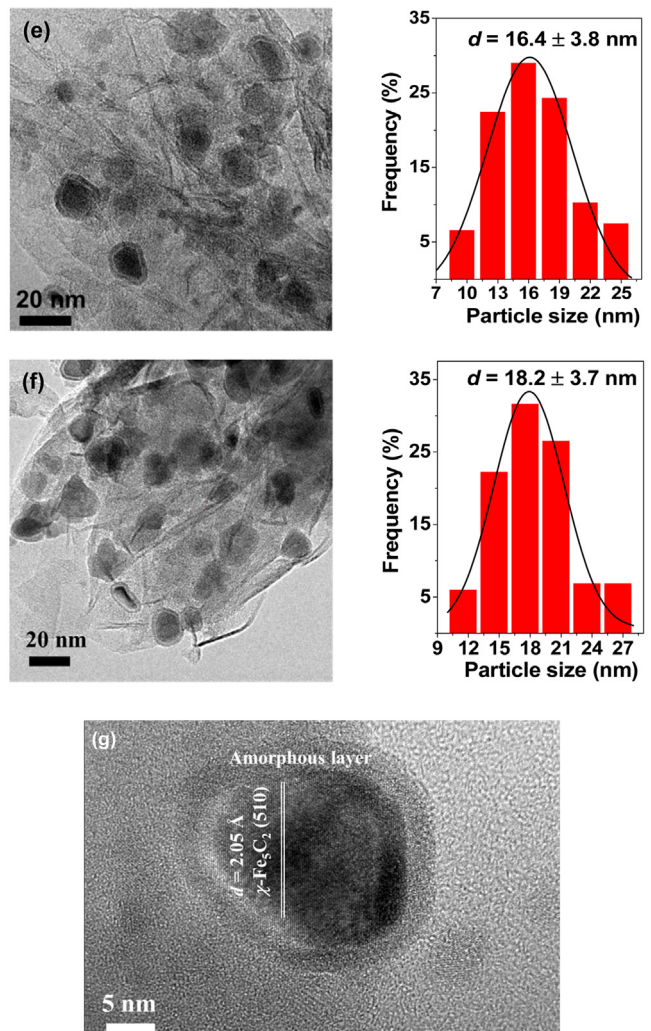


Fig. 8. (Continued)

rer equation, the crystallite size of $\chi\text{-Fe}_5\text{C}_2$ on FeMgK5/rGO was estimated to be 20.6 nm.

The TEM images and PSD histograms of these catalysts after 24 h on stream in FTO are shown in **Fig. 8**. It is observed that the particle size of $\chi\text{-Fe}_5\text{C}_2$ was 15.6 nm on Fe/rGO, which decreased to 13.9 nm on FeMg/rGO, as being carried over from the effect of Mg on the size of $\alpha\text{-Fe}_2\text{O}_3$ on the as-prepared Fe/rGO (**Fig. 4**). The particle size then grew gradually from 14.6 to 18.2 nm with the amount of K from 0.50 to 5.0 wt%. On FeMgK5/rGO, the particle size of $\chi\text{-Fe}_5\text{C}_2$ measured by TEM is in reasonable agreement with the crystallite size of $\chi\text{-Fe}_5\text{C}_2$ estimated by XRD, manifesting that the $\chi\text{-Fe}_5\text{C}_2$ NPs are single crystalline. The relatively small and highly dispersed $\chi\text{-Fe}_5\text{C}_2$ NPs after 24 h on stream in FTO at 613 K is ascribed to the presence of abundant defects (**Fig. S1**) and oxygen-containing groups (**Fig. S2**) including C=O, C=O, and O=C=O groups [46,47] on rGO, which functioned as the anchorage sites for NPs and retarded particle aggregation at high temperature [13,48]. **Fig. 8** also reveals that most $\chi\text{-Fe}_5\text{C}_2$ NPs were covered by an amorphous shell of $\sim 2.0\text{--}3.0$ nm in thickness. **Fig. 8g** presents the HRTEM image of FeMgK2/rGO after 24 h on stream, which clearly discloses a single-crystalline core–amorphous shell structure. The lattice fringes throughout the core with the spacing of 2.05 Å are readily assigned to the (510) planes of $\chi\text{-Fe}_5\text{C}_2$, while the amorphous shell with low contrast may be ascribed to carbon deposits and/or amorphous iron carbides. It was reported that car-

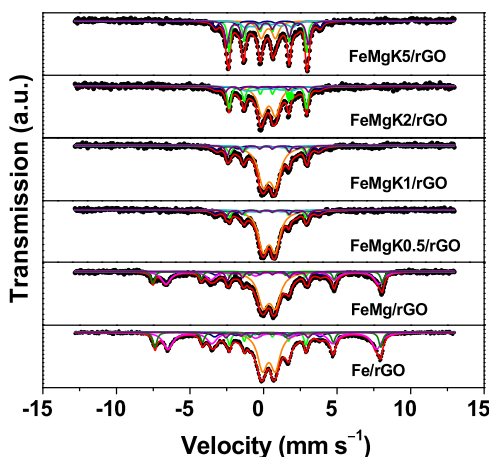


Fig. 9. ^{57}Fe Mössbauer spectra of the Fe/rGO, FeMg/rGO, and FeMgK/rGO catalysts after 24 h on stream in FTO.

bon deposits are not negligible especially under the FTO conditions characterized by high temperature and low H_2/CO ratio [49].

Fig. 9 presents the ^{57}Fe Mössbauer spectra of the Fe/rGO, FeMg/rGO, and FeMgK/rGO catalysts after 24 h on stream in FTO and the corresponding deconvoluted sub-spectra. The detailed fitting parameters are summarized in Table 3. The spectrum of Fe/rGO is best-fitted by one doublet and six sextets. The doublet with the IS of ca. 0.36 mm s^{-1} and the QS of ca. 0.88 mm s^{-1} is assigned to the superparamagnetic (spm) Fe(II) or Fe(III) species due to the presence of some poorly crystallized iron oxides [50]. Among six sextets, two sextets with the IS values of 0.60 and 0.30 mm s^{-1} and the H values of 44.1 and 47.7 T are attributed to the tetrahedral (A site) and octahedral sites (B site) of magnetite [51,52]. $\chi\text{-Fe}_5\text{C}_2$ is validated by three sextets with the H values of 16.2, 22.3, and 9.6 T [1,6]. Interestingly, one sextet with the IS of 0.17 mm s^{-1} and the H of 17.4 T attributable to $\epsilon'\text{-Fe}_{2,2}\text{C}$ [53] was also resolved in the present case, which has not been reported on the iron-based catalysts after FTO and has only been reported sporadically in FTS [32,54,55]. Usually, $\epsilon'\text{-Fe}_{2,2}\text{C}$ is stable at <473 K [53]. At higher temperatures, this iron carbide is inclined to transform into $\chi\text{-Fe}_5\text{C}_2$ or catalytically inactive cementite ($\theta\text{-Fe}_3\text{C}$) [56]. It is conceivable that the low H_2/CO ratio for FTO and the carbonaceous rGO support are conducive to an environment of high carbon potential (μ_{C}) [56], thus favoring the formation and stabilization of $\epsilon'\text{-Fe}_{2,2}\text{C}$ at as high as 613 K. Since $\epsilon'\text{-Fe}_{2,2}\text{C}$ was not identified by XRD and HRTEM, it is likely that this iron carbide exists in an amorphous form.

According to Table 3, the content of iron carbides ($\chi\text{-Fe}_5\text{C}_2 + \epsilon'\text{-Fe}_{2,2}\text{C}$) was 23.0% on Fe/rGO, which declined to 21.2% on FeMg/rGO. After decorating FeMg/rGO with K, the content of iron carbides increased steadily from 33.6 to 82.5% with the amount of K from 0.50 to 5.0 wt%. By plotting the content of iron carbides against the CO_2 adsorption capacity derived from CO_2 -TPD (Fig. S3), a linear relationship is obtained for the FeMg/rGO and FeMgK/rGO catalysts (Fig. 10), indicating that the extent of carburization is critically determined by the surface basicity of the catalysts, as also observed previously on the K-decorated Fe/rGO catalysts [13].

4. Discussion

Consistent with the present work, Luo and Davis [15] and Li and co-workers [16] reported that CO_2 was mitigated when the iron-based catalysts were decorated with Mg in FTS, which was attributed to the inhibitive effect of Mg on the WGS reaction. According to Iglesia and co-workers, CO_2 is produced in two reaction pathways during FTS [8]. The primary pathway is the reaction of the co-adsorbed CO (CO^*) with the chemisorbed oxygen atoms

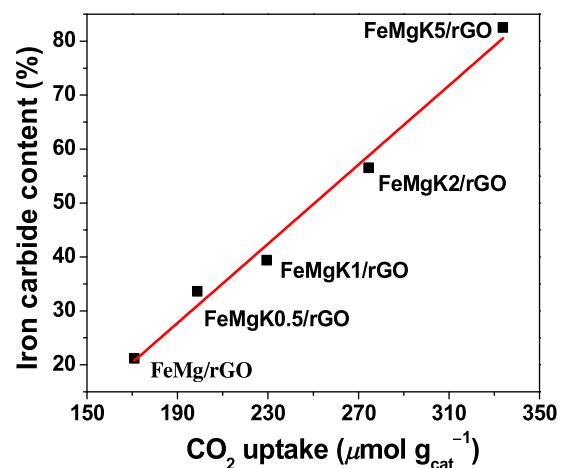


Fig. 10. Plot of the content of iron carbides as a function of the surface basicity of the FeMg/rGO and FeMgK/rGO catalysts.

(O^*) formed in the CO dissociation steps, and the secondary pathway is the WGS reaction. It is acknowledged that magnetite is the most active phase for WGS among the iron-containing phases formed during FTS [57,58], while the Fe(II) and Fe(III) cations are far less active [59]. The XRD (Fig. 7) and ^{57}Fe MAS results (Fig. 9 and Table 3) of the Fe/rGO and FeMg/rGO catalysts reveal that the content of magnetite decreased from 43.8 to 37.9% after Mg decoration. Meanwhile, the CO_2 selectivity decreased from 49.7 to 40.7%. This coherence may be taken as a direct evidence that supports the speculation that Mg lowers the CO_2 selectivity by inhibiting the WGS reaction [15,16]. It is interesting that although further decoration with only 0.50 wt% of K on FeMg/rGO almost completely depleted magnetite, the CO_2 selectivities on the dual-decorated FeMgK/rGO catalysts remained identical to that on FeMg/rGO. This result may be rationalized by hypothesizing the formation of a magnetite–iron carbides core–shell structure on FeMg/rGO during FTO, which is a well-accepted structure model for the activated iron-based catalysts in FTS [60], considering that the surface of the iron-based catalysts tends to be preferentially carburized. In addition, this result, as well as the identical CO_2 selectivity on Fe/rGO and FeK2/rGO (Table 2), hints that K did not affect either the primary pathway or the secondary pathway for the generation of CO_2 at least within the amounts of K investigated or under the FTO reaction conditions.

The ^{57}Fe Mössbauer results show that Mg decoration slightly reduced the extent of carburization of Fe/rGO. Although successive decoration with K did not affect the selectivity to CO_2 , it improved the extent of carburization. The contents of iron carbides follow the order of FeMg/rGO < Fe/rGO < FeMgK0.5/rGO < FeMgK1/rGO, which is qualitatively consistent with the order of their FTYS, suggesting that iron carbides are the active phases for FTO. In the literature, only $\chi\text{-Fe}_5\text{C}_2$ was identified after FTO and ascribed as the active phase [1,13,24,28]. Currently, we cannot distinguish the individual contributions of $\chi\text{-Fe}_5\text{C}_2$ and $\epsilon'\text{-Fe}_{2,2}\text{C}$ to the FTO activity, because it is difficult to prepare a $\epsilon'\text{-Fe}_{2,2}\text{C}$ -dominant catalyst that is stable at the high temperature for FTO [56]. Increasing the amount of K to 2.0 and 5.0 wt% did not improve the FTYS further (Table 2) despite of the fact that the contents of iron carbides kept on increasing, which may be explained by the coverage of the active sites by excessive K [61]. In addition, the alkali metal promoters such as Na and K are inclined to induce carbon deposition [22,32,62], which blocks the active sites and leads to further activity drop.

The endeavor to correlate the activity with the content of iron carbides (Fig. S4) turns out that the FTYS of FeMgK0.5/rGO, FeMgK1/rGO, and FeMgK2/rGO deviated substantially from the lin-

Table 3⁵⁷Fe Mössbauer parameters of the Fe/rGO, FeMg/rGO, and FeMgK/rGO catalysts after 24 h on stream in FTO.^a

Catalyst	IS (mm s ⁻¹)	QS (mm s ⁻¹)	H (T)	Γ (mm s ⁻¹)	Phase ascription	A (%)
Fe/rGO	0.36	0.88	—	0.78	Fe(II)/Fe(III)	33.2
	0.24	0.08	16.2	0.27	χ -Fe ₅ C ₂ (A)	8.6
	0.24	0.05	22.3	0.58	χ -Fe ₅ C ₂ (B)	6.4
	0.34	0.02	9.6	0.35	χ -Fe ₅ C ₂ (C)	2.9
	0.60	—	44.1	0.78	Fe ₃ O ₄ (A)	32.3
	0.30	—	47.7	0.31	Fe ₃ O ₄ (B)	11.5
FeMg/rGO	0.17	0.15	17.4	0.38	ε' -Fe _{2,2} C	5.1
	0.40	0.84	—	0.86	Fe(II)/Fe(III)	40.9
	0.24	0.08	16.0	0.26	χ -Fe ₅ C ₂ (A)	4.8
	0.24	0.14	22.2	0.58	χ -Fe ₅ C ₂ (B)	6.0
	0.34	0.02	9.6	0.43	χ -Fe ₅ C ₂ (C)	2.3
	0.61	—	45.0	0.74	Fe ₃ O ₄ (A)	28.0
	0.28	—	48.5	0.28	Fe ₃ O ₄ (B)	9.9
FeMgK0.5/rGO	0.23	0.12	17.1	0.30	ε' -Fe _{2,2} C	8.1
	0.39	0.82	—	0.78	Fe(II)/Fe(III)	66.4
	0.25	0.08	16.0	0.23	χ -Fe ₅ C ₂ (A)	8.4
	0.25	0.01	21.7	0.51	χ -Fe ₅ C ₂ (B)	9.4
	0.34	0.02	10.0	0.67	χ -Fe ₅ C ₂ (C)	6.4
FeMgK1/rGO	0.20	0.10	17.2	0.30	ε' -Fe _{2,2} C	9.4
	0.40	0.83	—	0.85	Fe(II)/Fe(III)	60.6
	0.25	0.10	16.1	0.35	χ -Fe ₅ C ₂ (A)	12.0
	0.28	0.04	21.5	0.54	χ -Fe ₅ C ₂ (B)	9.9
	0.34	0.02	10.0	0.64	χ -Fe ₅ C ₂ (C)	6.0
FeMgK2/rGO	0.22	0.10	17.0	0.28	ε' -Fe _{2,2} C	11.5
	0.36	0.92	—	0.70	Fe(II)/Fe(III)	43.5
	0.25	0.10	16.3	0.26	χ -Fe ₅ C ₂ (A)	26.9
	0.28	0.01	21.8	0.58	χ -Fe ₅ C ₂ (B)	8.3
	0.34	0.11	10.0	0.80	χ -Fe ₅ C ₂ (C)	13.4
FeMgK5/rGO	0.15	0.19	17.5	0.29	ε' -Fe _{2,2} C	7.9
	0.33	0.97	—	0.55	Fe(II)/Fe(III)	17.5
	0.25	0.09	16.4	0.24	χ -Fe ₅ C ₂ (A)	28.1
	0.28	0.04	22.0	0.41	χ -Fe ₅ C ₂ (B)	10.5
	0.31	0.11	10.0	0.60	χ -Fe ₅ C ₂ (C)	14.1
	0.22	0.12	17.2	0.33	ε' -Fe _{2,2} C	29.8

^a IS, isomer shift (relative to α -Fe); QS, quadrupole shift for sextet or quadrupole splitting for doublet; H, hyperfine magnetic field; Γ , FWHM; A, relative spectral area.

ear relationship, showing that some factor other than the content of iron carbides is affecting the activity. As the activity enhancements reported on the K-decorated Mn/FeN/CNT catalyst [25] and the Fe/rGO catalyst with comparable content of iron carbide [13] in FTO are far less prominent than that on the Mg and K dual-decorated Fe/rGO catalysts, both Mg and K should be responsible for the drastic activity enhancement. Note that in both the surface carbide mechanism and the surface enol mechanism for FTS, the dissociation of CO is crucial [53]. CO adsorbs via Fe–C σ -bonding and the simultaneous back-donation of iron valence electrons into the antibonding $2\pi^*$ orbitals of carbon in CO. In the presence of basic promoter(s), the Fe–C bond is strengthened and the C–O bond is weakened due to enhanced back-donation [45]. Hence, the direct dissociation (surface carbide mechanism) or the H₂-aided dissociation (surface enol mechanism) of the C–O bond is promoted [45,53,63–65], which affords more carbon building blocks for FTO and hence higher activity. Therefore, we tentatively propose that the promoted dissociation of CO by the combined effect of Mg and K is responsible for the unprecedentedly high activity on the dual-decorated FeMgK/rGO catalysts. On FeMgK5/rGO, excess K may lead to larger domains of the promoter with poor contact between the promoter and iron carbides [66], thus weakening the promotion effect.

5. Conclusions

The decoration of Fe/rGO with Mg is effective in mitigating CO₂ generation and improving carbon efficiency in FTO, which is attributed to the suppression of the formation of the WGS-active

magnetite phase. The shortcomings of Mg decoration, i.e., low activity and low selectivity to light olefins, are amended by subsequent decoration with K, while favorably preserving the beneficial effect of Mg. The promotion effect of K on the carburization of iron and the combined effect of Mg and K on the dissociation of CO are proposed to be responsible for the unprecedentedly high activity of the Mg and K dual-decorated Fe/rGO catalysts. This work demonstrates for the first time that using a combination of Mg and K as the promoters, it is viable to obtain an iron-based catalyst that exhibits high carbon efficiency, high activity, and high selectivity to light olefins in the industrially significant FTO reaction.

Acknowledgements

This work was supported by the National Natural Science Foundation of China (21373055), the National Basic Research Program of China (2012CB224804, 2016YFB0301602), the Science and Technology Commission of Shanghai Municipality (08DZ2270500), the Beijing Synchrotron Radiation Facility (BSRF), and the Shanghai Synchrotron Radiation Facility (SSRF). M.H.Q. thanks Dr. A. I. Dugulan of Utrecht University for his instructive suggestions about the fitting of ε' -Fe_{2,2}C in catalysts after FTO.

Appendix A. Supplementary data

Supplementary data associated with this article can be found, in the online version, at <http://dx.doi.org/10.1016/j.apcatb.2016.11.058>.

References

- [1] H.M.T. Galvis, J.H. Bitter, C.B. Khare, M. Ruitenbeek, A.I. Dugulan, K.P. de Jong, *Science* 335 (2012) 835–838.
- [2] F. Jiao, J.J. Li, X.L. Pan, J.P. Xiao, H.B. Li, H. Ma, M.M. Wei, Y. Pan, Z.Y. Zhou, M.R. Li, S. Miao, J. Li, Y.F. Zhu, D. Xiao, T. He, J.H. Yang, F. Qi, Q. Fu, X.H. Bao, *Science* 351 (2016) 1065–1068.
- [3] K. Cheng, B. Gu, X.L. Liu, J.C. Kang, Q.H. Zhang, Y. Wang, *Angew. Chem. Int. Ed.* 55 (2016) 4725–4728.
- [4] B.X. Hu, S. Frueh, H.F. Garces, L.C. Zhang, M. Aindow, C. Brooks, E. Kreidler, S.L. Suib, *Appl. Catal. B* 132–133 (2013) 54–61.
- [5] C.G. Visconti, M. Martinelli, L. Falbo, A. Infantes-Molina, L. Lietti, P. Forzatti, G. Iaquaniello, E. Palo, B. Picutti, F. Brignoli, *Appl. Catal. B* 200 (2017) 530–542.
- [6] H.M.T. Galvis, J.H. Bitter, T. Davidian, M. Ruitenbeek, A.I. Dugulan, K.P. de Jong, *J. Am. Chem. Soc.* 134 (2012) 16207–16215.
- [7] H.M.T. Galvis, K.P. de Jong, *ACS Catal.* 3 (2013) 2130–2149.
- [8] S. Krishnamoorthy, A. Li, E. Iglesia, *Catal. Lett.* 80 (2002) 77–86.
- [9] F.G. Botes, *Appl. Catal. A* 328 (2007) 237–242.
- [10] C. Pirola, C.L. Bianchi, A.D. Michele, S. Vitali, V. Ragaini, *Catal. Commun.* 10 (2009) 823–827.
- [11] C.F. Wang, X.L. Pan, X.H. Bao, *Chin. Sci. Bull.* 55 (2010) 1117–1119.
- [12] X.Q. Chen, D.H. Deng, X.L. Pan, X.H. Bao, *Chin. J. Catal.* 36 (2015) 1631–1637.
- [13] Y. Cheng, J. Lin, K. Xu, H. Wang, X.Y. Yao, Y. Pei, S.R. Yan, M.H. Qiao, B.N. Zong, *ACS Catal.* 6 (2016) 389–399.
- [14] M.K. Niemelä, A.O.I. Krause, *Catal. Lett.* 34 (1995) 75–84.
- [15] M.S. Luo, B.H. Davis, *Appl. Catal. A* 246 (2003) 171–181.
- [16] J. Yang, Y.C. Sun, Y. Tang, Y. Liu, H.L. Wang, L. Tian, H. Wang, Z.X. Zhang, H.W. Xiang, Y.W. Li, *J. Mol. Catal. A* 245 (2006) 26–36.
- [17] S. Stankovich, D.A. Dikin, R.D. Piner, K.A. Kohlhaas, A. Kleinhannmes, Y. Jia, Y. Wu, S.T. Nguyen, R.S. Ruoff, *Carbon* 45 (2007) 1558–1565.
- [18] K. Xu, Y. Cheng, J. Lin, H. Wang, S.H. Xie, Y. Pei, S.R. Yan, M.H. Qiao, Z.H. Li, B.N. Zong, *J. Catal.* 339 (2016) 102–110.
- [19] M.K. Niemelä, A.O.I. Krause, T. Vaara, V.J. Lahtinen, *Top. Catal.* 2 (1995) 45–57.
- [20] J.Z. Lu, L.J. Yang, B.L. Xu, Q. Wu, D. Zhang, S.J. Yuan, Y. Zhai, X.Z. Wang, Y.N. Fan, Z. Hu, *ACS Catal.* 4 (2014) 613–621.
- [21] J.F. Li, X.F. Cheng, C.H. Zhang, Y. Yang, Y.W. Li, *J. Mol. Catal. A* 396 (2015) 174–180.
- [22] H.M.T. Galvis, A.C.J. Koeken, J.H. Bitter, T. Davidian, M. Ruitenbeek, A.I. Dugulan, K.P. de Jong, *J. Catal.* 303 (2013) 22–30.
- [23] X.Q. Chen, D.H. Deng, X.L. Pan, Y.F. Hu, X.H. Bao, *Chem. Commun.* 51 (2015) 217–220.
- [24] H.J. Schulte, B. Graf, W. Xia, M. Muhler, *ChemCatChem* 4 (2012) 350–355.
- [25] Z.Q. Yang, X.L. Pan, J.H. Wang, X.H. Bao, *Catal. Today* 186 (2012) 121–127.
- [26] J.D. Xu, K.T. Zhu, X.F. Weng, W.Z. Weng, C.J. Huang, H.L. Wan, *Catal. Today* 215 (2013) 86–94.
- [27] X.P. Zhou, J. Ji, D. Wang, X.Z. Duan, G. Qian, D. Chen, X.G. Zhou, *Chem. Commun.* 51 (2015) 8853–8856.
- [28] H.M.T. Galvis, A.C.J. Koeken, J.H. Bitter, T. Davidian, M. Ruitenbeek, A.I. Dugulan, K.P. de Jong, *Catal. Today* 215 (2013) 95–102.
- [29] M. Casavola, J. Hermannsdörfer, N. de Jonge, A.I. Dugulan, K.P. de Jong, *Adv. Funct. Mater.* 25 (2015) 5309–5319.
- [30] D. Wang, X.P. Zhou, J. Ji, X.Z. Duan, G. Qian, X.G. Zhou, D. Chen, W.K. Yuan, *J. Mater. Chem. A* 3 (2015) 4560–4567.
- [31] L.P. Han, C.Z. Wang, G.F. Zhao, Y. Liu, Y. Lu, *AIChE J.* 62 (2016) 742–752.
- [32] Y. Yang, H.W. Xiang, Y.Y. Xu, L. Bai, Y.W. Li, *Appl. Catal. A* 266 (2004) 181–194.
- [33] N. Lohitharn, J.G. Goodwin Jr., *J. Catal.* 260 (2008) 7–16.
- [34] Y. Liu, J.F. Chen, J. Bao, Y. Zhang, *ACS Catal.* 5 (2015) 3905–3909.
- [35] Q.H. Zhang, J.C. Kang, Y. Wang, *ChemCatChem* 2 (2010) 1030–1058.
- [36] M.E. Dry, J.A.K. du Plessis, G.M. Leuteritz, *J. Catal.* 6 (1966) 194–199.
- [37] S.Z. Li, G.D. Meitzner, E. Iglesia, *J. Phys. Chem. B* 105 (2001) 5743–5750.
- [38] M. Zhang, B.H. Qu, D.N. Lei, Y.J. Chen, X.Z. Yu, L.B. Chen, Q.H. Li, Y.G. Wang, T.H. Wan, *J. Mater. Chem.* 22 (2012) 3868–3874.
- [39] S. Altieri, S.F. Contri, S. Agnoli, S. Valeri, *Surf. Sci.* 566–568 (2004) 1071–1075.
- [40] A.R. Siamaki, A.E.R.S. Khder, V. Abdelsayed, M.S. El-Shall, B.F. Gupton, *J. Catal.* 279 (2011) 1–11.
- [41] J.L. Rankin, C.H. Bartholomew, *J. Catal.* 100 (1986) 533–540.
- [42] J. Lahtinen, J. Vaari, A. Talo, A. Vehanen, P. Hautojärvi, *Surf. Sci.* 245 (1991) 244–254.
- [43] C.H. Zhang, G.Y. Zhao, K.K. Liu, Y. Yang, H.W. Xiang, Y.W. Li, *J. Mol. Catal. A* 328 (2010) 35–43.
- [44] H.J. Wan, B.S. Wu, H.W. Xiang, Y.W. Li, *ACS Catal.* 2 (2012) 1877–1883.
- [45] D.G. Miller, M. Moskovits, *J. Phys. Chem.* 92 (1988) 6081–6085.
- [46] G.J. Wu, X.M. Wang, N.J. Guan, L.D. Li, *Appl. Catal. B* 136–137 (2013) 177–185.
- [47] M. Gopiraman, S.G. Babu, Z. Khatri, W. Kai, Y.A. Kim, M. Endo, R. Karvembu, I.S. Kim, *J. Phys. Chem. C* 117 (2013) 23582–23596.
- [48] S.O. Moussa, L.S. Panchakarla, M.Q. Ho, M.S. El-Shall, *ACS Catal.* 4 (2014) 535–545.
- [49] A.C.J. Koeken, H.M.T. Galvis, T. Davidian, M. Ruitenbeek, K.P. de Jong, *Angew. Chem. Int. Ed.* 51 (2012) 7190–7193.
- [50] K. Xu, B. Sun, J. Lin, W. Wen, Y. Pei, S.R. Yan, M.H. Qiao, X.X. Zhang, B.N. Zong, *Nat. Commun.* 5 (2014) 5783.
- [51] N. Sirimanathan, H.H. Hamdeh, Y.Q. Zhang, B.H. Davis, *Catal. Lett.* 82 (2002) 181–191.
- [52] B. Sun, J. Lin, K. Xu, Y. Pei, S.R. Yan, M.H. Qiao, X.X. Zhang, B.N. Zong, *ChemCatChem* 5 (2013) 3857–3865.
- [53] E. de Smit, B.M. Weckhuysen, *Chem. Soc. Rev.* 37 (2008) 2758–2781.
- [54] J.A. Amelse, J.B. Butt, L.H. Schwartz, *J. Phys. Chem.* 82 (1978) 558–563.
- [55] G.B. Raupp, W.N. Delgass, *J. Catal.* 58 (1979) 348–360.
- [56] E. de Smit, F. Cinquini, A.M. Beale, O.V. Safonova, W. van Beek, P. Sautet, B.M. Weckhuysen, *J. Am. Chem. Soc.* 132 (2010) 14928–14941.
- [57] D.C. Grenoble, M.M. Estadt, D.F. Ollis, *J. Catal.* 67 (1981) 90–102.
- [58] R.J. Madon, W.F. Taylor, *J. Catal.* 69 (1981) 32–43.
- [59] D.G. Rethwisch, J.A. Dumesic, *J. Catal.* 101 (1986) 35–42.
- [60] S.Z. Li, W.P. Ding, G.D. Meitzner, E. Iglesia, *J. Phys. Chem. B* 106 (2002) 85–91.
- [61] D.B. Bokur, D. Mukesh, S.A. Patel, *Ind. Eng. Chem. Res.* 29 (1990) 194–204.
- [62] W.P. Ma, E.L. Kugler, D.B. Dadyburjor, *Energy Fuels* 21 (2007) 1832–1842.
- [63] M.E. Dry, T. Shingles, L.J. Boshoff, G.J. Oosthuizen, *J. Catal.* 15 (1969) 190–199.
- [64] G. Brodén, G. Gafner, H.P. Bonzel, *Surf. Sci.* 84 (1979) 295–314.
- [65] J. Benziger, R.J. Madix, *Surf. Sci.* 94 (1980) 119–153.
- [66] S.Z. Li, S. Krishnamoorthy, A.W. Li, G.D. Meitzner, E. Iglesia, *J. Catal.* 206 (2002) 202–217.